Faraday Discussions

Cite this: DOI: 10.1039/d5fd00177c

PAPER

Exploring the orientation of a PAS-domain protein at model protein interfaces with distinct secondary-structure content across nano- and micro-scales

Montserrat Román Quintero, [ab] Mark Mero, [c] Alexander Veber, [bd] Ljiljana Puskar, [d] András Dér, [e] Ferenc Bogár [f] and Zsuzsanna Heiner *[ab]

Received 22nd December 2025, Accepted 17th February 2026
DOI: 10.1039/d5fd00177c

While electrostatic interactions often drive protein adsorption at biointerfaces, the influence of the underlying secondary structure of the scaffold remains poorly understood. In this study, we compare the adsorption of photoactive yellow protein (PYP) onto three positively charged model protein surfaces: a rigid, planar β-sheet scaffold, a three-dimensional α-helical scaffold, and their (αβ) mixture, by using controlled pH and temperature adjustments to impose distinct secondary structures of poly-L-lysine. Using chiral and achiral vibrational sum-frequency generation (VSFG) and nano-FTIR spectroscopy, we demonstrate that the β-sheet surface promotes the formation of a well-defined monolayer with a signature β-scaffold peak at 1627 and 1680 cm^{-1}. In contrast, the α-helical surface induces a multilayering effect, resulting in a five-fold enhancement of the chiral signal and the emergence of a prominent broad feature at 1654 cm^{-1}, assigned to a chiral hydration network trapped within the protein assembly. Our results reveal that the 3D 'brush-like' topography of the helical surface provides superior orientational templating compared to the planar β-sheet, forcing the PYP molecules into a near-perfect vertical alignment. This work highlights that the conformational architecture of a biointerface is as critical as its chemical functionality in governing protein orientation and hydration at the nanoscale.

[a]School of Analytical Sciences Adlershof, Humboldt-Universität zu Berlin, Albert-Einstein-Straße 5-9, 12489 Berlin, Germany. E-mail: zsuzsanna.heiner@hu-berlin.de
[b]Department of Chemistry, Humboldt-Universität zu Berlin, Brook-Taylor-Straße 2, 12489 Berlin, Germany
[c]Max Born Institute for Nonlinear Optics and Short Pulse Spectroscopy, 12489 Berlin, Germany
[d]Institute for Electronic Structure Dynamics, Helmholtz-Zentrum Berlin für Materialien und Energie GmbH, Albert-Einstein-Straße 15, 12489 Berlin, Germany
[e]HUN-REN Biological Research Centre, Institute of Biophysics, H-6726 Szeged, Hungary
[f]HUN-REN-SZTE Biomimetic Systems Research Group, Hungarian Research Network, University of Szeged, H-6720 Szeged, Hungary

Introduction

Proteins rarely function alone. In the crowded, watery environment of a cell, they encounter various charged interfaces formed by membranes, cytoskeletal filaments, and supramolecular structures. At these boundaries, the physicochemical conditions differ significantly from those in the surrounding bulk: electrostatic fields, hydrogen-bond networks, and steric constraints establish unique orientations and secondary-structure patterns that affect key biological processes such as signal transduction, enzymatic catalysis, and complex assembly. Over the past decade, increased awareness of protein misfolding disorders, including amyloidosis and neurodegenerative diseases,[1,2] has emphasized the importance of understanding how proteins interact with complex, heterogeneous, and partially ordered environments. As a result, a detailed, site-specific characterization of protein conformations and orientations at interfaces is crucial for both fundamental biochemistry and the rational design of biomaterials, implants, and optoelectronic devices. However, determining the secondary structure and orientation of protein molecules in ultrathin interfacial films remains a significant experimental challenge.

For protein layers approximately 10 nm thick supported on polymeric substrates, many established structural probes either lack sufficient sensitivity or are not inherently specific to interfaces. Scattering techniques such as neutron and X-ray reflectometry offer valuable data on layer thickness, density, and interfacial roughness, but do not provide direct information on molecular conformation or vibrational signatures related to protein secondary structure. Conversely, vibrational spectroscopic methods such as vibrational sum-frequency generation (VSFG) spectroscopy, nanoscale Fourier-transform infrared (nano-FTIR) spectroscopy, and polarization-modulated infrared reflection-absorption spectroscopy (PM-IRRAS) can directly probe amide vibrational modes, thereby revealing details of secondary structure and molecular orientation.

PM-IRRAS can also provide additional orientational insights. However, applying it to protein films at air–dielectric interfaces is difficult because of the low infrared reflectivity of dielectric substrates and the weak signals produced, which often require careful optical modeling and limit sensitivity for ultrathin layers. Additionally, on dielectric substrates, the vibrational band positions in IRRAS are influenced not only by polarization and electrodynamic boundary conditions but also by the oscillator strength of the vibration.[3] In contrast, VSFG spectroscopy is uniquely interface-specific and well suited for ultrathin films,[4] while nano-FTIR spectroscopy enables spatially resolved analysis on the nanometre scale.[5,6] Additionally, chiral VSFG spectroscopy exhibits unique sensitivity to molecular chirality[7,8] and protein secondary structure,[9,10] comparable to other chiroptical vibrational spectroscopic techniques, such as Raman optical activity[11] and vibrational circular dichroism.[12,13]

The photoactive yellow protein (PYP) of Halorhodospira halophila exemplifies a well-characterised, water-soluble globular photoreceptor that is increasingly considered for bioelectronic and integrated-optics applications[14,15] and is extensively used as a model of PAS-family proteins. A 14 kDa, 125-residue protein, PYP adopts the canonical PAS domain fold: a central β-sheet bounded by α-helical connectors and hydrophobic cores. At the same time, its surface is decorated with

alternating patches of positive and negative charge that mediate solvent interactions. The light-responsive chromophore of the protein and its conserved α/β scaffold render PYP an attractive model for studying signal transduction, protein–protein interactions, and surface-induced conformational changes. Despite extensive structural characterisation of PYP in the bulk by X-ray crystallography and NMR,[16–21] the interfacial behaviour of the protein remains largely unexplored.

Layer-by-layer (LbL)-assembled polyelectrolyte multilayers (PEMs) provide a versatile platform for generating defined, tunable interfacial environments that mimic biological interfaces.[22–24] Poly-L-lysine (PLL)-based PEMs are particularly attractive due to the pH-, ionic-strength-, and temperature-dependent secondary-structure transitions of PLL, enabling systematic variation of interfacial charge density, hydration, and mechanical stiffness. By integrating PYP into such multilayer architectures, one can probe how subtle changes in the nanoscale interfacial landscape modulate protein adsorption, orientation, and folding pathways, yielding insights that are directly relevant to the design of protein-based biomaterials, the understanding of protein aggregation in disease, and the optimization of bio-optical devices. Moreover, the natural binding partner of PYP remains unknown, providing further motivation to explore how PYP responds to interfaces of varying structural order.

In this study, a multilayer LbL architecture was fabricated, with the terminal PLL layer deliberately conditioned *via* controlled pH and temperature adjustments to impose distinct secondary structures at the interface. Following the adsorption of PYP onto this final layer, we aimed to elucidate how the protein responds to these differing structural environments and to assess whether it exhibits preferential orientation under specific conditions. To this end, we employed a multiscale characterization strategy: atomic force microscopy (AFM) to probe nanoscale morphology, VSFG spectroscopy to provide molecular-level insight into the interface, and nano-FTIR spectroscopy with imaging to examine protein structure with 25 nm spatial resolution. The secondary structural contents of the bulk samples were also determined by circular dichroism (CD) spectroscopy. All in all, these complementary approaches were designed to reveal possible orientational changes and adsorption properties of PYP at model protein interfaces induced by the underlying secondary structure of PLL.

Methods

The multilayers were prepared using the LbL method,[25] in which polymer solutions were sequentially sprayed onto argon-plasma-cleaned CaF_2 windows for VSFG studies and onto Si wafers for nano-FTIR measurements. As a polymer multilayer separates the solid support from the protein film, protein adsorption, orientation, and secondary structure are governed by the polymer's surface chemistry rather than by the underlying CaF_2 or Si substrate. We note that while the use of silicon as a solid support is well established and advantageous for nano-FTIR measurements, this substrate choice results in a reduced sensitivity of the nano-FTIR configuration to in-plane molecular vibrations compared to VSFG measurements using CaF_2.[26]

Initially, five μL of branched polyethylenimine (PEI, Sigma-Aldrich, Mw: 600 000–1 000 000) at a concentration of 5 mg mL^{-1} was applied to the substrates.

After 5 minutes, the substrates were rinsed with Millipore water. Subsequently, six pairs of layers of poly-L-glutamic acid (PGA, Sigma Aldrich, Mw: 50 000–100 000 with sodium salt) and poly-L-lysine (PLL, Sigma Aldrich >30 000 with hydrobromide), each at a concentration of 1 mg mL^{-1}, were sequentially sprayed so that a PLL layer followed the negatively charged PGA layer (Fig. S1). Previous studies have demonstrated that polymer multilayers comprising six or more layer pairs are needed to achieve a laterally uniform surface suitable for subsequent protein adsorption.[22,27–29] Between each layer, a waiting time was required to ensure stabilization and the polyelectrolyte's adsorption to the surface before washing with water and proceeding to the next layer. For all purposes, Milli-Q ultrapure water (18.2 MΩ cm) was used, which was filtered through a 0.22 μm Millipore membrane filter before use.

For PLL, three distinct bulk samples, referred to as PLL_β, PLL_α, and $PLL_{\alpha\beta}$ were prepared under three different microenvironmental conditions: (i) pH 7, 23 °C; (ii) pH 11, 23 °C; and (iii) pH 11, 60 °C, respectively. The α and β labels indicate that the dominant secondary structures of the respective samples, as determined by CD spectroscopy in the bulk phase using an available web server,[30,31] are α-helical and β-sheet, respectively. The pH of the PLL stock solution was adjusted with 1 M NaOH using pH test strips, and the temperature of $PLL_{\alpha\beta}$ was raised to 60 °C to promote β-like aggregate formation. In the multilayer assemblies, PLL_β was used for all PLL layers, except for the topmost layer, where the secondary structure was varied by using PLL_β, PLL_α, or $PLL_{\alpha\beta}$. This approach enabled the preparation of charged topmost PLL layers with varying secondary-structure contents. At the same time, washing/rinsing maintained a near-physiological pH on the surface of the topmost layer after its adsorption.

For the preparation of wild-type PYP (expressed in *Escherichia coli*), the method described in the literature[32,33] was employed. The PYP layer was deposited on the topmost PLL layer in the $PEI(PGA\text{-}PLL)_6$ assembly by pipetting 280 μM of PYP stock solution, then washing it out after 5 minutes. On the three different PLL topmost layers, three samples with PYP were prepared, named after the PLL layers, *i.e.*, PYP-PLL_β, PYP-PLL_α, and PYP-$PLL_{\alpha\beta}$. The samples were stored in a custom-built sample holder to maintain a relative humidity above 50% and were left to equilibrate for 1 hour before any measurements. The LbL method yielded nanometer-scale layer thicknesses, both with and without PYP, as confirmed by AFM measurements (Fig. S2 and S3 in the SI).

Vibrational sum-frequency generation spectroscopy

A detailed description of the custom-built broadband VSFG spectrometer has been reported elsewhere,[34,35] so only a summary of the relevant experimental details is provided here. A 100 kHz, 6 W Yb:$KGd(WO_4)_2$ laser oscillator-amplifier system operating at 1028 nm powered the entire setup. The pump pulses were split into two arms: one produced narrowband near-infrared (NIR) pulses at 1028 nm with a pulse energy of 0.55 μJ, and the other generated broadband mid-infrared (IR) pulses tunable from 1000 to 2200 cm^{-1}. For the current measurements, the 1500–1700 cm^{-1} range was selected with a pulse energy of 0.22 μJ to cover the amide I spectral region. To reduce atmospheric water vapor absorption in the IR beamline, a laboratory-built purge box was used to maintain a dry airflow. The IR and NIR beams overlapped in time and space at the interface, and

the SFG signal was collected with a spectrograph fitted with a Peltier-cooled CCD (Fig. 1). The spectral resolution was limited by the bandwidth of the narrowband pulse, which had a spectral width of 5 cm^{-1}.[34] The VSFG spectra were obtained in the SSP (achiral) and SPP (chiral) polarization combinations. For each polarization combination, data were collected from three independently prepared samples for both systems (PLL alone and PYP adsorbed on PLL), with measurements taken at 20 distinct lateral positions per sample. The acquisition times were 40 s for SSP and 60 s for SPP, and the entire set of experiments was repeated at least three times, all conducted at room temperature (23 °C).

After frequency calibration, the difference spectra were obtained by subtracting the background spectrum recorded without IR excitation. A non-resonant (NR) reference spectrum was measured on a gold (111) surface and normalized to the applied infrared intensity. The corrected NR spectrum was then used to normalize each difference spectrum for the respective polarization combination. The calibrated VSFG spectra (effective $|\chi^{(2)}|^2$) were averaged and used for further analysis. Next, the imaginary component of the effective $\chi^{(2)}$ spectrum was retrieved using the maximum entropy method (MEM),[36,37] which provided the Lorentzian resonance frequencies and the likely relative signs of their amplitudes. These parameters were then used as initial values to fit the normalized VSFG spectra with a sum of Lorentzian functions:

$$I_{\mathrm{VSFG}}(\omega) \propto \left| A_{\mathrm{NR}}\, e^{i\Phi} + \sum_{i=1}^{\nu} \frac{Q_\nu}{\omega - \omega_\nu - i\Gamma_\nu} \right|^2 . \quad (1)$$

The first term on the right expresses the frequency-independent nonresonant (NR) contribution with amplitude A_{NR} and phase Φ. The second term is a sum of resonant Lorentzian terms associated with vibrational modes. Q_ν represents the amplitude, ω_ν is the frequency, and Γ_ν is the damping factor of the ν-th Lorentzian resonance. Fabry–Perot interference arising from thin-film effects was neglected

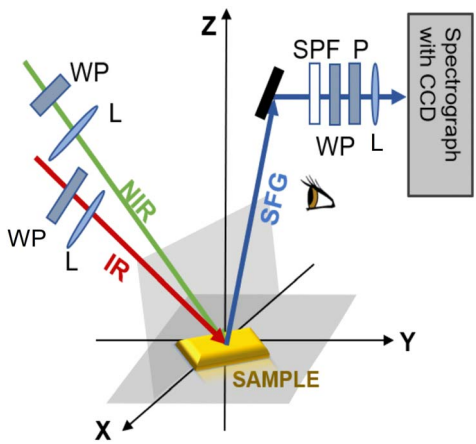

Fig. 1 Schematic VSFG spectroscopic setup in the laboratory frame (*X*, *Y*, *Z*). L: lens, WP: half-wave plate, P: polarizer, SPF: short-pass filter.

in the data analysis, as the optical thickness of the samples was sufficiently small relative to the laser wavelengths.

Infrared nanospectroscopy and imaging

The experiments were carried out at the IR-nanospectroscopy end-station of the IR beamline at the BESSY II storage ring.[38] The setup features an s-SNOM (neaScope, Attocube GmbH, Germany) connected to the broadband infrared synchrotron light (Fig. 2).[39] Measurements were performed using a Pt-Ir-coated AFM probe with a tip radius of 25 nm operated in tapping mode, with a tapping amplitude of approximately 70 nm and a resonance oscillation frequency of about 266 kHz (Arrow™ NCPt, NanoWorld, Neuchâtel, Switzerland). For IR nano-imaging, the so-called white-light (zero-path-difference heterodyne) imaging mode was employed, using broadband infrared synchrotron radiation collected simultaneously with mechanical topography. The nano-FTIR spectra were obtained by positioning the AFM tip at a designated point (see Fig. 4 and 6) and recording spectra within the 800–2100 cm^{-1} range at a nominal spectral resolution of $\leq$8 cm^{-1}. The acquisition time was 12 minutes for a single spatial location, during which 10 spectra were averaged, resulting in averaged spectra from 12, 35, and 5 similar regions of interest for PLL_{β}, PLL_{α}, and $PLL_{\alpha\beta}$, respectively. The same applies to the PYP case. A background spectrum was collected from a clean Si wafer and averaged over 20 spectra, resulting in 42 minutes of acquisition time.

The recorded interferograms were converted to phase and amplitude spectra using an in-house script from the IRIS beamline, employing an asymmetric apodization window based on the Blackman–Harris function. The measured spectra were then referenced to a bare silicon surface and subsequently baseline-corrected to determine the relative phase-shift spectra corresponding to the infrared response of the molecular-layer assembly. The optical detector signal was demodulated at the second harmonic of the AFM cantilever oscillation frequency to reduce far-field background effects, thereby isolating the near-field amplitude (O2A) and phase (O2P) used for image and spectral reconstruction.

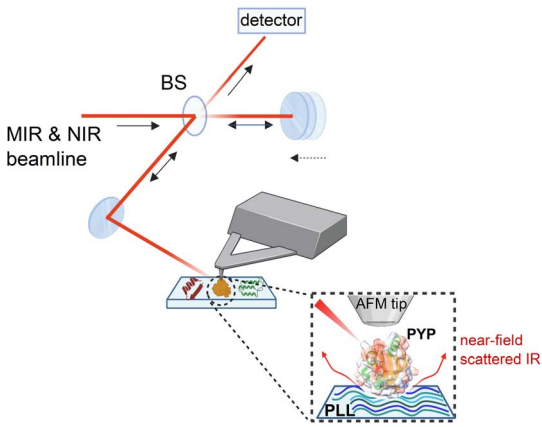

Fig. 2 Schematic representation of the nano-FTIR based on the s-SNOM technique. Figure created using BioRender.

Simultaneously acquired s-SNOM channels, including topography, mechanical phase, and optical amplitude, were processed using Gwyddion.[40] All measurements were performed at ambient temperature under continuous dry nitrogen purging, with the s-SNOM instrument operated inside an acoustically isolated enclosure.

Results and discussion

PLL interface with different secondary structural contents probed by VSFG and nano-FTIR spectroscopy

Fig. 3 displays the measured chiral VSFG spectra of PLL recorded in the amide I region and the topographic images recorded by AFM. The corresponding achiral VSFG spectra are shown in Fig. S4a. Additionally, for each case, the imaginary parts of the chiral VSFG spectra were retrieved using MEM (Fig. S5). Afterwards, the VSFG spectra were fitted using eqn (1). A summary of the chiral VSFG band assignments is shown in Table S1.

As shown in Fig. 3a, PLL_β displays fibrillar structures characteristic of both α-helices and β-sheet structures. However, the VSFG spectrum (Fig. 3d and e_1) indicates that PLL_β forms a well-ordered β-sheet structure, which resulted in the B2 mode at 1625 cm^{-1} and the B1 mode at 1676 cm^{-1}. The chiral O–H bending mode at 1648 cm^{-1} is visible throughout the entire measurement range. While the amplitude of the chiral amide II vibrational mode is minimal, a notable

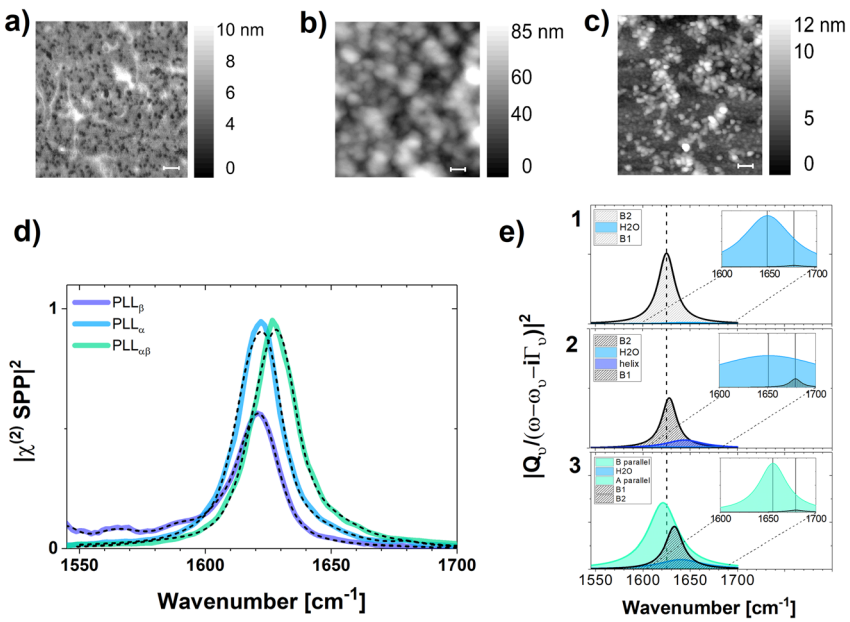

Fig. 3 AFM topography images of 2 × 2 μm^2 areas of multilayer structures with a topmost layer of (a) PLL_β, (b) PLL_α, and (c) $PLL_{\alpha\beta}$. Scale bars: 200 nm. Tip radius of the AFM: 10 nm. (d) Chiral VSFG spectra of PLL with their respective fitting curves (dashed lines, based on eqn (1)), acquired at an acquisition time of 60 seconds in each case. (e) Component Lorentzian bands of the VSFG spectra, where the bands are exemplified by colored curves. The rectangle is used to illustrate a zoom in the B_1 mode. Numbers 1, 2, and 3 on (e) indicate the topmost PLL layer as PLL_β, PLL_α, and $PLL_{\alpha\beta}$, respectively.

contribution was obtained in the achiral VSFG spectra (Fig. S4a), which can be attributed to the presence of a partial β-fibril structure. Our results are similar to those obtained by Strazdaite *et al.* in the amide II region for β-fibrillar structures.[41] It is noteworthy that our CD experiments (Fig S6) show that in the fully charged state of PLL at pH 7 (PLL_β), ∼48% of the polypeptide chain is characterized by β-sheet secondary structure, ∼15% forms turn structures, and the remaining ∼37% of the chain remains unfolded. Based on earlier observations, this ratio in the PLL secondary structure is related to the strong electrostatic repulsion between neighboring charged groups, which forces the polypeptide to elongate rather than to form a fibrillar structure.[42,43] In contrast, oligomeric and fibrillar structures of PLL were previously observed only at pH levels above 9.[44] These results highlight how polymer behavior can change when adsorbed onto a surface, with differences that may differ from those in the bulk phase.

Importantly, when the pH was increased to 11 in the bulk (PLL_α), the topography of the film changed sharply, as shown in Fig. 3b. Under these conditions, PLL predominantly forms spherical structures with an average diameter of about 50–80 nm. Based on VSFG spectra (Fig. 3d and e_2), these changes can be linked to the presence of α-helices at 1644 cm^{-1} and β-sheet structures (B2 mode at 1628 cm^{-1}, and B1 mode at 1679 cm^{-1}). To the best of our knowledge, this work reports the first observation of a chiral VSFG band associated with a helical secondary structure. The amplitude of the Lorentzian fit for the α-helical band at 1644 cm^{-1} (E1 mode) indicates a high percentage of this structure at the interface. Likewise, the CD spectrum of PLL_α (Fig. S6) shows that the α-helix is the dominant secondary structure (25.8%) in the bulk phase. This strong chiral VSFG signal for helices can be expected only if the surface organization breaks in-plane symmetry, *i.e.*, directional or chiral packing, as suggested by the topography image (Fig. 3b). It should be noted that the O–H bending mode exhibits a slight blue shift in the presence of helical structures in comparison to PLL_β. This behavior indicates that interfacial water molecules near the helices remain strongly hydrogen-bonded, but changes in surface charge cause a shift in peak position. This observation appears to be linked to the positively charged side chains of PLL, which strongly modulate the hydrogen-bond strength of interfacial water. In contrast, strong broadening of the O–H bending mode was obtained for PLL_α, which reflects a broader range of chiral hydration motifs. We attribute this broadening to the mixed orientational distribution of the chiral O–H bending mode of α-helices and β-sheet structures.

When $PLL_{\alpha\beta}$ served as the topmost layer, as shown in Fig. 3c, we observed the formation of smaller spherical aggregates with diameters below 40 nm compared with the PLL_α sample, and these aggregates were more widely spaced across the surface. Examining Fig. 3d and e_3, we noticed a slight shift of the B2 (1633 cm^{-1}) mode of the antiparallel β-sheet to higher wavenumbers, and a substantial downshift to 1640 cm^{-1} and peak narrowing of the O–H bending mode. We also observed a new band at 1655 cm^{-1}. Although turn structures exhibit a characteristic amide I vibrational frequency near 1660 cm^{-1}, their contribution to the chiral VSFG signal is expected to be negligible. The CD spectrum of bulk $PLL_{\alpha\beta}$ is in good agreement with the chiral VSFG results, indicating a high content of β-sheet conformations, but it also reveals the presence of α-helical structure (∼21%) in a larger proportion than turn structures (7.7%). However, our data do not support the formation of fibrillar aggregates with an α-helix-rich conformation

under the environmental conditions employed to prepare the bulk solution, as previously inferred from FTIR and TEM measurements.[44] Notably, both the interface VSFG and the bulk CD spectra of PLL showed an increased abundance of parallel sheets (19%), whose spectral signatures were observed at 1621 and 1655 cm^{-1} in both chiral and achiral VSFG spectra. These two peaks, characteristic of a parallel sheet, were also previously observed in hIAPP aggregates.[45]

Finally, it is essential to note that the film thickness depends on the secondary structure of the topmost PLL layer. For example, the PLL_{β} layer is thinner than the PLL_{α} layer (Fig. S2a and b), indicating that the side chains of the polyelectrolytes are fully ionized, and a very thin monolayer of PLL is formed on the topmost surface of the multilayer structure. As the pH increased in the bulk, the formation of an unordered, gauche-rich hydrocarbon side chain likely induced α-helical conformations (PLL_{α}) that adsorbed onto the film surface, accompanied by a thickening of the adsorbed layer (Fig. S2b). However, $PLL_{\alpha\beta}$ regained its ionized state, likely due to the introduction of highly ordered *trans*-rich hydrocarbon side chains, which adopted parallel and antiparallel β-sheet structures (Fig. S2c), resulting again in the formation of a monolayer of PLL.

Fig. 4 presents the white-light optical images, the nano-FTIR spectra covering the 900–1760 cm^{-1} spectral range for films with differently prepared PLL topmost layers, along with the corresponding second derivative spectra. As shown in the near-field optical amplitude image (Fig. 4a), the PLL_{β} sample exhibits a surface morphology characterized by a worm-like structure with a distinct near-field scattering distribution. The spectral data show that the amide I (1600–

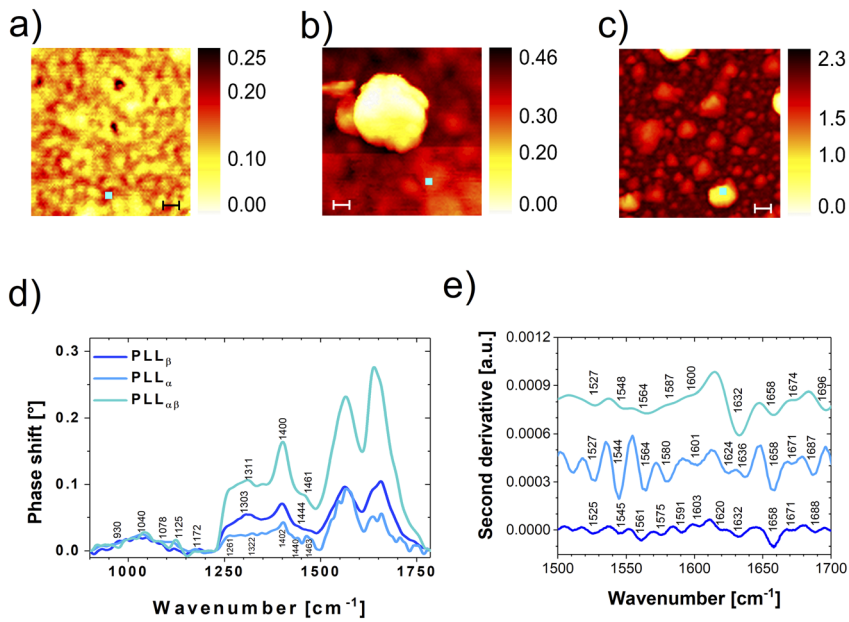

Fig. 4 Near-field optical amplitude demodulated at the second harmonic of the tapping frequency (O2A) images retrieved for (a) PLL_{β}, (b) PLL_{α}, and (c) $PLL_{\alpha\beta}$. Image area: 1 × 1 μm^2. Scale bar: 100 nm. The blue dots represent where the data was collected. (d) Corresponding nano-FTIR spectra of PLL and their respective (e) second derivatives and band assignments. Tip radius was 25 nm.

1700 cm^{-1}) and amide II (1510–1580 cm^{-1}) spectral features are the most prominent, and a strong peak around 1400 cm^{-1} (symmetric stretching mode of COO^-) is also characteristic of each sample.

In Fig. 4e, the second derivative spectrum of PLL_β is shown at the bottom of the graph, with the corresponding vibrational band assignments summarized in Table S3. The spectra reveal the presence of the NH_3^+ groups of the charged side chain group of PLL (1525 and 1620 cm^{-1}), α-helices (1658 cm^{-1}), as well as turn structures (1671 cm^{-1}), and antiparallel β-sheet formations (1632 and 1688 cm^{-1}). Compared with the VSFG spectra acquired for the same sample, only slight frequency upshifts are observed. However, a key difference is the detection of α-helical and turn features, which were not resolved in the VSFG spectra recorded using the SPP and SSP polarization combinations. We attribute these differences to (i) film dehydration effects during the long measurement times, which can cause helix formation, as was observed earlier for intrinsically unordered proteins using FTIR spectroscopy,[46] and (ii) detection of turns with chiral VSFG spectroscopy requires a very high degree of interfacial orientational order, which is usually rare in polyelectrolytes. Furthermore, the ~10 cm^{-1} shifts in wavenumber can be attributed to differences in the molecular response functions probed by VSFG (hyperpolarizability) and FTIR (dipole tensor). Similar shifts have previously been observed for amino acids using surface-enhanced Raman *versus* hyper-Raman spectroscopy, where the selection rules of the two methods also differ.[47] In contrast, the amide II modes acquired with nano-FTIR showed no shift in their spectral position. These observations can also be attributed to the intrinsic sensitivity of the nano-FTIR technique to out-of-plane vibrational modes.[48] In contrast, VSFG spectroscopy yields in-plane (SSP polarization) modes and chiral secondary structural features only under conditions of high structural ordering.

The second-derivative spectrum of PLL_α (Fig. 4e) reveals NH_3^+ vibrational modes at 1527 and 1624 cm^{-1}, and β-sheet structures at 1636 and 1687 cm^{-1}, with frequencies that show almost no shift relative to the PLL_β sample. In contrast, the amide I and amide II modes (turns and α-helices) display much higher amplitudes than in PLL_β. The O2A image (Fig. 4b) shows large, closely packed spherical aggregates, similar to those visible in the AFM image (Fig. 3b). Notably, the nano-FTIR spectral features are consistent with the corresponding VSFG spectra. Additionally, for PLL_α, the band at 1658 cm^{-1} exhibits the highest amplitude, indicating the highest helical content, in agreement with the VSFG results.

In the final case, $PLL_{\alpha\beta}$, β-sheet features (1632 and 1696 cm^{-1}) dominate the spectrum (Fig. 4e), with only a slight blueshift of the antiparallel B1 mode relative to PLL_β, while the other amide I and II modes remain at the same positions. The image in Fig. 4c shows spherical aggregates again, with a more noticeable difference in near-field scattering between the granulates. In summary, these results demonstrate that the combination of chiral VSFG and nano-FTIR spectroscopy can be used to identify nanoscale secondary structural contents of adsorbed macromolecules at biointerfaces.

PYP on different secondary structures of PLL using VSFG and nano-FTIR spectroscopy

After establishing the properties of the three thin multilayer films with various PLL topmost layers, we now describe how PYP adsorbs differently on those layers.

Fig. 5 shows the topography measured by AFM, and the corresponding chiral VSFG spectra of PYP adsorbed on the topmost PLL surface in the amide I region. The related achiral VSFG spectra are displayed in Fig. S4b. The imaginary parts of the VSFG spectra for each condition (Fig. S7) were retrieved using MEM, and the VSFG spectra were fitted using eqn (1). A summary of the chiral VSFG band assignments is shown in Table S2.

Compared to PLL, PYP exhibits a different topography. In Fig. 5a, when PYP is adsorbed on PLL_{β}, larger and relatively homogeneous PYP islands are evenly distributed across the surface, with very few observable aggregates. These aggregates are probably due to α-helices in the PYP structure, as indicated by Lorentzian bands seen in Fig. $5e_1$ and their VSFG spectra in Fig. 5d. The Lorenzian band profiles in Fig. $5e_1$ reveal a high abundance of β-sheet structures, with B2 and B1 amide I modes at 1627 cm^{-1} and 1679 cm^{-1}, respectively, along with α-helices at 1660 cm^{-1}, which differ significantly from PLL_{β} alone. Based on our bulk CD spectroscopic results (Fig. S6), the structural composition of PYP is ~10% helical content, 33% sheets, 15% turns, and the remaining part is other/unordered. Given the typical uncertainties of CD deconvolution (±5–10% per category, especially for β-rich, chromophore-containing proteins), our CD values are broadly consistent with the known structure of PYP based on the protein data

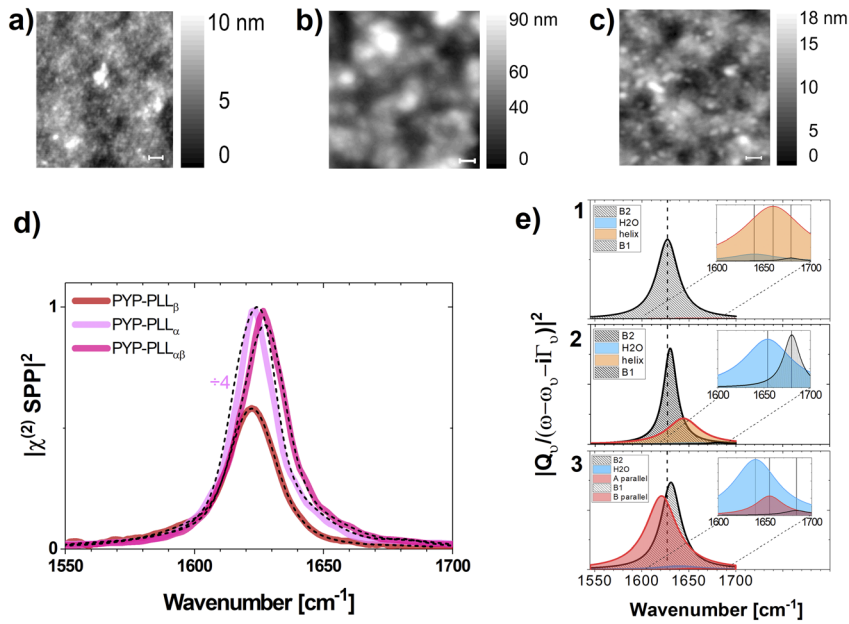

Fig. 5 AFM topography images of 2 × 2 μm^2 areas of PYP on the surface of (a) PLL_{β}, (b) PLL_{α}, and (c) $PLL_{\alpha\beta}$. Scale bars: 200 nm. Tip radius of the AFM: 10 nm. (d) Chiral VSFG spectra with their respective fitting curves (dashed lines) of PYP adsorbed on PLL_{β}, PLL_{α}, and $PLL_{\alpha\beta}$ surfaces. Acquisition time for cases PYP-PLL_{β} and PYP-$PLL_{\alpha\beta}$: 60 s; for PYP-PLL_{α}: 15 s (this curve is divided by 4 to maintain the scale). (e) Component Lorentzian bands for each of the VSFG spectra, where the bands are exemplified by colored curves. The rectangle is used to illustrate a zoom in the B_1 mode region of the graphs. Numbers 1, 2, and 3 on (e) indicate the topmost structure of PLL_{β}, PLL_{α}, and $PLL_{\alpha\beta}$, respectively, on which PYP adsorbed.

bank (PDB) entries PDB 1NWZ and 3PHY. It is noteworthy that the chiral VSFG signal from the α-helical regions of PYP is observed only when PYP is adsorbed on the PLL_β surface, as seen in SPP polarization. In contrast, the VSFG spectrum recorded in SSP polarization combination (Fig. S4b) shows band shifts within the range of 1640–1650 cm^{-1} and an amplitude increase at 1660 cm^{-1} compared to the PLL_β surface, likely because of the presence of helical units in PYP, and/or a change in the nonresonant contribution.[49] While Yan *et al.* reported that α-helical structures do not give rise to a chiral amide I band,[50] Ishibashi and co-workers observed a small but significant chiral amide I mode for bovine serum albumin (BSA).[51] Our results further suggest that chiral VSFG modes associated with helical units can be detected when a PAS-family protein and its subunits are highly oriented at surfaces.

When PYP is adsorbed on the PLL_α surface, the topography in Fig. 5b indicates elongated aggregates where PYP accumulates, forming large islands with lateral dimensions exceeding 200 nm. Simultaneously, the surface heterogeneity and the peak-to-valley height variations observed in the AFM topography and phase images are significantly reduced following PYP adsorption, as evidenced by comparison of Fig. S8c and d with Fig. S9c and d. As shown in Fig. 3d and e_2, these large aggregates are characteristic of α-helix formation, indicated by the band at 1644 cm^{-1} (E mode of the helix), which is also detected for PLL_α but with a much smaller amplitude. In addition, β-sheet structures remain clearly discernible through the B1 (1680 cm^{-1}) and B2 (1630 cm^{-1}) modes, with their amplitudes increasing following PYP adsorption on the PLL_α surface. At the same time, the O–H bending mode at 1654 cm^{-1} narrowed relative to that of PLL_α alone, which can be attributed to the more restricted secondary and tertiary structure of PYP, causing a more ordered and homogeneous chiral water structure than that associated with PLL_α.

Previous studies have shown that water molecules can organize into chiral assemblies around proteins, with the handedness of the hydration structure reflecting the biomolecule's intrinsic chirality[52,53] Moreover, chiral VSFG spectroscopy has been demonstrated to be a unique approach for selectively probing the vibrational signatures of water in the first hydration shell at biomolecular interfaces.[54] Given that random coil and turn motifs are not expected to generate measurable chiral VSFG responses, and that the 1650 cm^{-1} band decreases in amplitude upon PYP adsorption while all amide I features increase, we assign this resonance to a hydration-related interfacial contribution rather than to protein backbone vibrations. The pronounced narrowing of this band upon adsorption, *i.e.*, the linewidth changed from 160 to 60 cm^{-1}, suggests a reorganization of the chiral hydration structure at the interface, consistent with a more uniform hydration environment associated with the adsorbed protein layer. The reduced linewidth and amplitude of this band relative to the PLL-only case indicate a more homogeneous and constrained hydration environment, consistent with water in the protein hydration shell.

When PYP is adsorbed onto $PLL_{\alpha\beta}$, as shown in Fig. 5c, smaller aggregates can be observed. While Fig. 5d and e_3 show almost no shift in the amide I region, the band at 1644 cm^{-1} detected for PYP-PLL_α disappears, and a new feature emerges at 1655 cm^{-1} for PYP-$PLL_{\alpha\beta}$. When comparing PYP-$PLL_{\alpha\beta}$ with PYP-PLL_β, the bands characteristic of the amide I B modes of β-sheets and the O–H bending mode exhibit very similar features. However, PYP adsorbed on the $PLL_{\alpha\beta}$ surface

shows an increased β-sheet contribution, which is probably due to the underlying PLL surface rather than to the protein.

To obtain additional spectral information from highly localized areas, nano-FTIR measurements were performed across the 800–2700 cm^{-1} spectral range at specific positions on the nanoscale films, *i.e.*, those selected in the white-light images (Fig. 6a–c). A detailed analysis of the spectra in the 900–1750 cm^{-1} region was then conducted, and its second derivatives in the amide I and II regions were determined to identify PYP-related features. Fig. 6 presents nano-FTIR spectra of PYP on PLL with different secondary-structure contents. In Fig. 6a, the O2A image of PYP on PLL_{β} reveals the presence of large aggregates that stand out from the homogeneous surface, on which only a few small aggregates are visible. Their corresponding nano-FTIR spectrum is shown in Fig. 6d, and the second derivative spectrum in Fig. 6e provides insight into their vibrational bands. As seen, the symmetric bending of the NH_3^+ group (1529 cm^{-1}), amide II bands (1546 and 1561 cm^{-1}), amide I of β-sheet (1637 and 1688 cm^{-1}), and turns (1664 cm^{-1}) are present. The spectra show contributions from the symmetric bending of the NH_3^+ group (1529 cm^{-1}), amide II bands (1546 and 1561 cm^{-1}), amide I modes of β-sheets (1637 and 1688 cm^{-1}), and turn-related features (1664 cm^{-1}). In contrast to PLL_{β} alone, the signature of helices is absent, and the vibrational modes between 1500 and 1700 cm^{-1} show only negligible shifts. In contrast, the amide III modes of PYP-PLL_{β} exhibit a characteristic shift from 1303 to 1315 cm^{-1}, associated with helices, and a new band at 1343 cm^{-1} upon PYP adsorption on the surface.

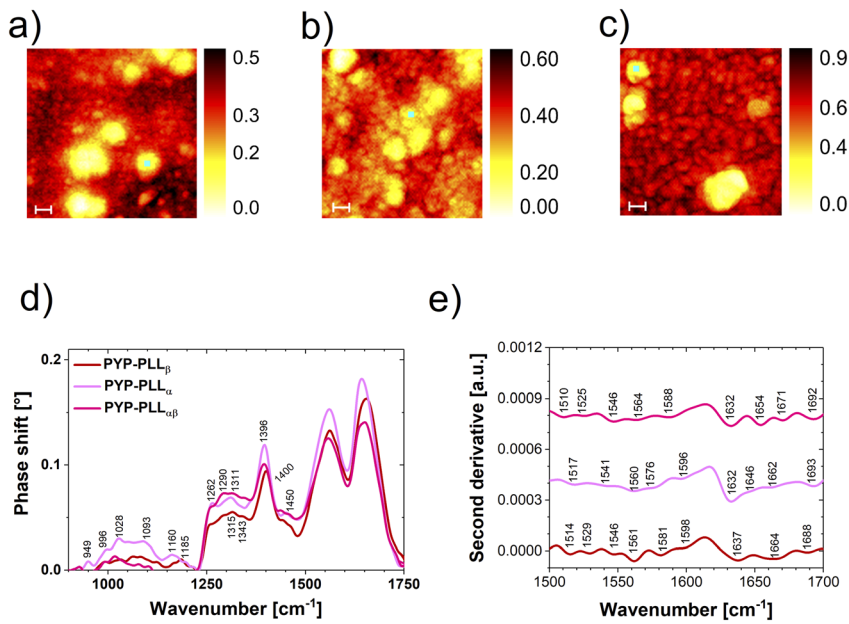

Fig. 6 Near-field optical amplitude demodulated at the second harmonic of the tapping frequency (O2A) images retrieved from nano-FTIR for PYP on the surface of (a) PLL_{β}, (b) PLL_{α}, and (c) $PLL_{\alpha\beta}$. Images of 1 × 1 μm^2 area. Scale bars: 100 nm. The blue dots represent where the data was collected. (d) Nano-FTIR spectra of PYP adsorbed on PLL_{β}, PLL_{α}, and $PLL_{\alpha\beta}$ surfaces and their respective (e) second derivatives and band assignments. Tip radius: 25 nm.

Furthermore, as shown in Fig. 6b, PYP adsorbed on PLL_{α} exhibits a more significant contribution from large aggregates distributed across the surface. This observation is consistent with the VSFG spectroscopy and AFM topography results discussed above, suggesting that this α-helix-rich surface supports the formation of a thicker PYP layer. Importantly, as seen in Fig. 6e, the symmetric and asymmetric bending modes of the NH_3^+ groups are absent. This can be a sign that PYP adsorption involves electrostatic interactions with the PLL moieties. However, the helix (1646 cm^{-1}) and β-sheet (1632 and 1693 cm^{-1}) components continue to contribute significantly, along with turns (1662 cm^{-1}). The decreased intensity of the helical features may be due to reorientation of the protein, such that PYP adopts a tilted orientation at nearly 45° relative to the surface. In contrast, the B2 mode associated with β-sheets increased in intensity compared with the other PYP layers. In addition, in the amide III region, the bands at 1322 and 1343 cm^{-1} observed for PLL_{α} disappear, while a strong, broad feature emerges at 1305 cm^{-1} upon PYP adsorption. This broad band may characterise the combined vibrations of the helical segments of PYP and their structural heterogeneity.

Furthermore, when PLL exhibits mixed secondary structures ($PLL_{\alpha\beta}$), as shown in Fig. 6c, PYP adsorbs efficiently onto the PLL surface. This surface resembles the topography presented in Fig. 5c, exhibiting small and large aggregates distributed across the surface, along with fewer larger aggregates. The second-derivative spectrum again shows significant contributions from the NH_3^+ band (1525 cm^{-1}), β-sheet modes (1632 and 1692 cm^{-1}), and the α-helical band (1654 cm^{-1}), along with a turn-related band (1671 cm^{-1}). However, when comparing PYP-$PLL_{\alpha\beta}$ with $PLL_{\alpha\beta}$, the vibrational modes in the amide I, II, and III regions are almost identical, except near 1600 cm^{-1}. In contrast, in the fingerprint region between 900 and 1100 cm^{-1}, all surfaces with a PLL topmost layer show characteristic bands at 930, 1040, and 1078 cm^{-1}, which can be assigned to skeletal C–C, side-chain C–N, and skeletal C–C stretching modes, respectively.

Upon PYP adsorption, new vibrational bands emerge (Fig. 7d): a C–C stretching or out-of-plane C–H bending feature (949 cm^{-1}), C–C stretching of chromophore or aromatic ring breathing modes (996 cm^{-1}), aromatic ring modes (1018/1028 cm^{-1}), and chromophore skeletal C–C or backbone C–O stretching modes (1093 cm^{-1}). Although these bands are typically associated with skeletal vibrations, we assign them to the *p*-coumaric acid chromophore, whose highly delocalized electronic structure can give rise to substantial changes in dipole moment.

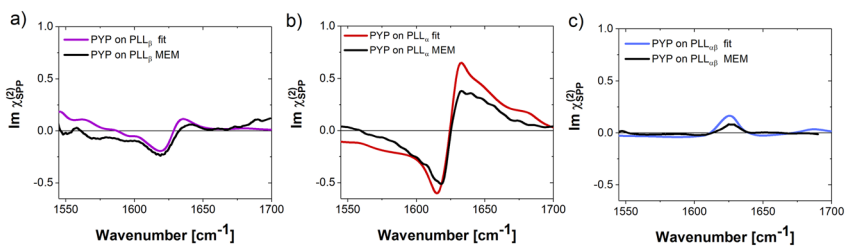

Fig. 7 Isolated $Im\chi^{(2)}$ spectra of PYP adsorbed on (a) PLL_{β}, (b) PLL_{α}, and (c) $PLL_{\alpha\beta}$ using the MEM algorithm and Lorentzian fit.

Finally, the PYP film thickness depends on pH, consistent with the trends we previously observed for PLL alone. For example, when PYP is adsorbed onto PLL_β, the resulting thickness is ≤20 nm, much lower than that of the other samples (Fig. S3). In contrast, the film thickness increases with the rise of α-helical content of PLL on the surface but decreases with increasing β-sheet formation. A densely packed and ordered PYP layer on PLL_α-terminated films is expected to result in a net positive surface charge, leading to further protein adsorption. This buildup process can thus repeat, forming a thick protein layer, as was previously reported for BSA adsorption on polyallylamine-terminated surfaces.[55] A very similar effect was observed when cells were attached to PLL top layers prepared at pH 10.4. The high adhesion of films formed under such conditions was attributed to the secondary structure and binding conformation of PLL[56] arising from its higher side-chain charge density. This approach therefore provides a rational design pathway and a model system for studying water-soluble protein adsorption at interfaces.

Unlike the homodyne intensity, $I_{VSFG} \propto |\chi^{(2)}|^2$, which contains cross-terms from interference (*cf.* eqn (1)), the imaginary part of the second-order nonlinear susceptibility is additive.[57,58] Therefore, the vibrational properties of the protein film can be isolated through subtraction of the spectrum retrieved for the bare PLL top layer from the spectrum extracted for the combined PLL-PYP layer assembly: $\mathrm{Im}[\chi_{PYP}^{(2)}] = \mathrm{Im}[\chi_{after}^{(2)}] - \mathrm{Im}[\chi_{before}^{(2)}]$. The validity and accuracy of this subtraction depend on several conditions and assumptions. As the thickness of the protein layer is much smaller than the coherence length of VSFG and the index of refraction of the LbL layer assembly is close to that of the PYP layer, no multiple reflections complicate the spectrum and the local field corrections (Fresnel factors) are unchanged during protein adsorption. Furthermore, the chiral handedness of the molecules making up both the LbL layer assembly and the PYP layer are known and identical. Therefore, the sign ambiguity in the MEM analysis due to the negligible nonresonant chiral background signal from CaF_2 can be resolved by forcing the *a priori* known sign of amide I modes in the retrieved imaginary parts. Finally, it must be assumed that the topmost PLL layer keeps its structural integrity upon PYP adsorption—a requirement

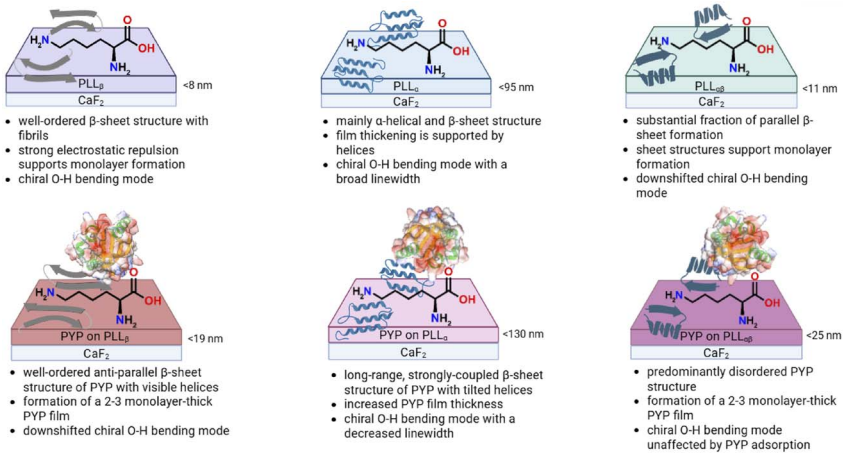

Fig. 8 Correlation between protein secondary structure and vibrational signatures on poly-L-lysine surfaces with different secondary structures.

that applies equally when using heterodyne-detected VSFG. The difference spectra, shown in Fig. 7, reveal distinct interfacial behaviour of PYP. The signature of the B_2 mode near 1620 cm^{-1} suggests that the protein exhibits an ordered anti-parallel β-sheet structure on PLL_β (*cf.* Fig. 7a). The characteristic antisymmetric derivative-like lineshape in Fig. 7b indicates that PYP adopts a long-range, excitonically even more strongly-coupled β-sheet on PLL_α than on PLL_β. This transition confirms that the 'soft' helical interface facilitates superior orientational templating. The emergence of a prominent broad feature at 1654 cm^{-1} (Fig. 7b) is assigned to a chiral hydration network trapped within the protein assembly. The observation that PYP on $PLL_{\alpha\beta}$ maintains a small but positive feature across the amide I region, but shifted to somewhat lower wavenumbers, is consistent with parallel β-sheet content and their reorientation toward a more parallel geometry with respect to the surface.

Conclusions

We have presented an integrated analytical approach that provides a rational framework for elucidating the adsorption behaviour of water-soluble and globular proteins at biointerfaces. The main findings are summarized in Fig. 8. Interfacial organization and protein secondary structure at model protein–protein interfaces were investigated using a combined spectroscopic strategy integrating AFM, VSFG, and nano-FTIR spectroscopy, together with near-field optical imaging. Layer-by-layer (LbL) assemblies terminated with PLL layers of tuneable secondary-structure content were employed as model platforms, with PYP serving as the target protein. Chiral VSFG spectra of PLL reveal pH- and temperature-dependent variations in secondary-structure composition within the amide I region, which are further corroborated by nano-FTIR measurements. By combining chiral and achiral VSFG spectroscopy with MEM analysis and peak fitting, chiral amide I E modes associated with helical units, B modes corresponding to antiparallel β-sheet structures, and both B and A modes characteristic of parallel β-sheet conformations were resolved. Upon adsorption of PYP onto PLL_α and PLL_β surfaces, distinct changes are observed in both the VSFG and nano-FTIR spectra, reflecting structure-dependent interactions at the protein–protein interface that manifest across the amide I, II, and III regions as well as the fingerprint region. In contrast, adsorption of PYP onto the $PLL_{\alpha\beta}$ surface results in no significant changes in the amide regions. Furthermore, the thickness of the adsorbed PYP layer is approximately 10 nm on PLL_β and $PLL_{\alpha\beta}$ surfaces, while increasing the α-helical content of PLL leads to thicker PYP films and enhanced β-sheet formation. Overall, this methodological advance establishes a robust foundation for the precise characterization required to address complex problems related to interfacial protein structure and function in materials science and biomedical applications.

Author contributions

MRQ: investigation, formal analysis, methodology, validation, visualization, writing. MM: software, methodology, formal analysis, writing. AV: software, methodology. LP: methodology, formal analysis. AD: methodology, conceptualization. FB: formal analysis, methodology, validation, writing. ZH: conceptualization, methodology, validation, investigation, software, resources, funding, writing, visualization, supervision.

Conflicts of interest

There are no conflicts to declare.

Data availability

The data supporting this article have been included as part of the supplementary information (SI). Supplementary information: Fig. S1: preparation of polyelectrolyte monolayers with and without PYP using the layer-by-layer (LbL) technique. Fig. S2: AFM images and height profiles on (a) PLL_{β}, (b) PLL_{α}, and (c) $PLL_{\alpha\beta}$. Fig. S3: AFM images and height profiles on PYP adsorbed on a topmost layer of (a) PLL_{β}, (b) PLL_{α}, and (c) $PLL_{\alpha\beta}$. Fig. S4: achiral VSFG spectra of a hydrated thin film of (a) PLL_{β}, PLL_{α}, and $PLL_{\alpha\beta}$ and (b) PYP on PLL_{β}, PLL_{α}, and $PLL_{\alpha\beta}$ on CaF_2. Fig. S5: imaginary part of the complex $\chi^{(2)}$ spectra of (a) PLL_{β}, (b) PLL_{α}, and (c) $PLL_{\alpha\beta}$ using the MEM algorithm and comparing it with the fitted curve. Fig. S6: CD spectra recorded using an Olis-DSM20 spectrophotometer. The structural motifs obtained from the fit are summarized in the table on the right side. Fig. S7: imaginary part of the complex $\chi^{(2)}$ spectra of PYP adsorbed on (a) PLL_{β}, (b) PLL_{α}, and (c) $PLL_{\alpha\beta}$ using the MEM algorithm and comparing it with the fitted curve. Fig. S8: mechanical amplitude and phase images of (a and b) PLL_{β}, (c and d) PLL_{α}, and (e and f) $PLL_{\alpha\beta}$, obtained with AFM. Fig. S9: mechanical amplitude and phase images of PYP adsorbed on (a and b) PLL_{β}, (c and d) PLL_{α}, and (e and f) $PLL_{\alpha\beta}$, obtained with AFM. Table S1: chiral VSFG vibrational mode assignments and corresponding fit parameters for VSFG spectroscopic results for PLL_{β}, PLL_{α}, and $PLL_{\alpha\beta}$. Table S2: chiral VSFG vibrational mode assignments and corresponding fit parameters for VSFG spectroscopic results for PYP on PLL_{β}, on PLL_{α}, and on $PLL_{\alpha\beta}$. Table S3: comparison of the tentative assignment of the vibrational bands observed in the spectra of PLL and PYP on PLL using nano-FTIR and VSFG spectroscopy, respectively. See DOI: https://doi.org/10.1039/d5fd00177c.

Acknowledgements

Z. H. acknowledges funding from the German Research Foundation (Deutsche Forschungsgemeinschaft, DFG) through the Julia Lermontova Fellowship (DFG GSC 1013 SALSA) and the Berliner Chancengleichheitsprogramm (BCP). M. R. Quintero further acknowledges support from the School of Analytical Sciences Adlershof (SALSA STF25-05). The authors also thank the Helmholtz-Zentrum Berlin für Materialien und Energie for granting synchrotron radiation beamtime at the IRIS beamline. A. V. and L. P. gratefully acknowledge funding by the German Federal Ministry for Education and Research (BMBF) project 05K19KH1 (SyMS). A. D. and F. B. are grateful to the National Research Development and Innovation Office of Hungary for the grant NKFI-1 ADVANCED 150958. Furthermore, the authors acknowledge the Core Facility BioSupraMol and K. Pagel at Freie Universität Berlin for providing access to the CD spectrophotometer, and they extend special thanks to E. Moon for her assistance in operating the machine. We also acknowledge the support of K. Balasubramanian, who provided access to the AFM.

Notes and references

1 A. Relini, N. Marano and A. Gliozzi, Misfolding of Amyloidogenic Proteins and Their Interactions with Membranes, *Biomolecules*, 2014, **4**(1), 20–55.
2 F. Chiti and C. M. Dobson, Protein Misfolding, Functional Amyloid, and Human Disease, *Annu. Rev. Biochem.*, 2006, **75**, 333–366.
3 C. Yang and C. Wöll, Infrared Reflection-Absorption Spectroscopy (IRRAS) applied to oxides: Ceria as a case study, *Surf. Sci.*, 2024, **749**, 122550.
4 X. D. Zhu, H. Suhr and Y. R. Shen, Surface vibrational spectroscopy by infrared-visible sum frequency generation, *Phys. Rev. B: Condens. Matter Mater. Phys.*, 1987, **35**(6), 3047–3050.
5 A. Centrone, Infrared Imaging and Spectroscopy Beyond the Diffraction Limit, *Annu. Rev. Anal. Chem.*, 2015, **8**, 101–126.
6 F. Keilmann, R. Hillenbrand, D. Richards and A. Zayats, Near-field microscopy by elastic light scattering from a tip, *Philos Trans R Soc Lond Ser Math Phys Eng Sci.*, 2004, **362**(1817), 787–805.
7 X. H. Hu, L. Fu, J. Hou, Y. N. Zhang, Z. Zhang and H. F. Wang, N–H Chirality in Folded Peptide LK7β Is Governed by the Cα–H Chirality, *J. Phys. Chem. Lett.*, 2020, **11**(4), 1282–1290.
8 M. Okuno and T. Ishibashi, Chirality Discriminated by Heterodyne-Detected Vibrational Sum Frequency Generation, *J. Phys. Chem. Lett.*, 2014, **5**(16), 2874–2878.
9 E. C. Y. Yan, L. Fu, Z. Wang and W. Liu, Biological Macromolecules at Interfaces Probed by Chiral Vibrational Sum Frequency Generation Spectroscopy, *Chem. Rev.*, 2014, **114**(17), 8471–8498.
10 W. Guo, T. Lu, Z. Gandhi and Z. Chen, Probing Orientations and Conformations of Peptides and Proteins at Buried Interfaces, *J. Phys. Chem. Lett.*, 2021, **12**(41), 10144–10155.
11 L. D. Barron, F. Zhu, L. Hecht, G. E. Tranter and N. W. Isaacs, Raman optical activity: An incisive probe of molecular chirality and biomolecular structure, *J. Mol. Struct.*, 2007, **834–836**, 7–16.
12 P. J. Stephens, Theory of vibrational circular dichroism, *J. Phys. Chem.*, 1985, **89**(5), 748–752.
13 T. A. Keiderling, Structure of Condensed Phase Peptides: Insights from Vibrational Circular Dichroism and Raman Optical Activity Techniques, *Chem. Rev.*, 2020, **120**(7), 3381–3419.
14 S. Krekic, M. Mero, A. Dér and Z. Heiner, Ultrafast All-Optical Switching Using Doped Chromoprotein Films, *J. Phys. Chem. C*, 2023, **127**(3), 1499–1506.
15 D. Petrovszki, S. Krekic, S. Valkai, Z. Heiner and A. Dér, All-Optical Switching Demonstrated with Photoactive Yellow Protein Films, *Biosensors*, 2021, **11**(11), 432.
16 U. K. Genick, G. E. O. Borgstahl, K. Ng, Z. Ren, C. Pradervand, P. M. Burke, *et al.*, Structure of a Protein Photocycle Intermediate by Millisecond Time-Resolved Crystallography, *Science*, 1997, **275**(5305), 1471–1475.
17 S. Anderson, S. Crosson and K. Moffat, Short hydrogen bonds in photoactive yellow protein, *Acta Crystallogr., Sect. D: Biol. Crystallogr.*, 2004, **60**(6), 1008–1016.

18 H. Ihee, S. Rajagopal, V. Šrajer, R. Pahl, S. Anderson, M. Schmidt, *et al.*, Visualizing reaction pathways in photoactive yellow protein from nanoseconds to seconds, *Proc. Natl. Acad. Sci. U. S. A.*, 2005, **102**(20), 7145–7150.

19 F. Schotte, H. S. Cho, F. Dyda and P. Anfinrud, Watching a signaling protein function: What has been learned over four decades of time-resolved studies of photoactive yellow protein, *Struct. Dyn.*, 2024, **11**(2), 021303.

20 F. Schotte, H. S. Cho, V. R. I. Kaila, H. Kamikubo, N. Dashdorj, E. R. Henry, *et al.*, Watching a signaling protein function in real time via 100-ps time-resolved Laue crystallography, *Proc. Natl. Acad. Sci. U. S. A.*, 2012, **109**(47), 19256–19261.

21 K. Pande, C. D. M. Hutchison, G. Groenhof, A. Aquila, J. S. Robinson, J. Tenboer, *et al.*, Femtosecond structural dynamics drives the trans/cis isomerization in photoactive yellow protein, *Science*, 2016, **352**(6286), 725–729.

22 I. V. Panayotov, P. Y. Collart-Dutilleul, H. Salehi, M. Martin, A. Végh, J. Yachouh, *et al.*, Sprayed Cells and Polyelectrolyte Films for Biomaterial Functionalization: The Influence of Physical PLL–PGA Film Treatments on Dental Pulp Cell Behavior, *Macromol. Biosci.*, 2014, **14**(12), 1771–1782.

23 M. H. Iqbal, H. Kerdjoudj and F. Boulmedais, Protein-based layer-by-layer films for biomedical applications, *Chem. Sci.*, 2024, **15**(25), 9408–9437.

24 J. J. Richardson, J. Cui, M. Björnmalm, J. A. Braunger, H. Ejima and F. Caruso, Innovation in Layer-by-Layer Assembly, *Chem. Rev.*, 2016, **116**(23), 14828–14867.

25 J. B. Schlenoff, S. T. Dubas and T. Farhat, Sprayed Polyelectrolyte Multilayers, *Langmuir*, 2000, **16**(26), 9968–9969.

26 I. Pascual Robledo, C. Maciel-Escudero, M. Schnell, L. Mester, J. Aizpurua and R. Hillenbrand, Theoretical Description of Infrared Near-Field Spectroscopy of In- and Out-of-Plane Molecular Vibrations in Thin Layers, *ACS Photonics*, 2025, **12**(7), 3782–3793.

27 C. Picart, G. Ladam, B. Senger, J. C. Voegel, P. Schaaf, F. J. G. Cuisinier, *et al.*, Determination of structural parameters characterizing thin films by optical methods: A comparison between scanning angle reflectometry and optical waveguide lightmode spectroscopy, *J. Chem. Phys.*, 2001, **115**(2), 1086–1094.

28 M. Michel, V. Toniazzo, D. Ruch and V. Ball, Deposition Mechanisms in Layer-by-Layer or Step-by-Step Deposition Methods: From Elastic and Impermeable Films to Soft Membranes with Ion Exchange Properties, *Int. Sch. Res. Not.*, 2012, **2012**(1), 701695.

29 I. Pelsöczi, K. Turzó, C. Gergely, A. Fazekas, I. Dékány and F. Cuisinier, Structural Characterization of Self-Assembled Polypeptide Films on Titanium and Glass Surfaces by Atomic Force Microscopy, *Biomacromolecules*, 2005, **6**(6), 3345–3350.

30 A. Micsonai, É. Bulyáki and J. Kardos, BeStSel: From Secondary Structure Analysis to Protein Fold Prediction by Circular Dichroism Spectroscopy, in *Structural Genomics*, ed. Chen Y. W. and Yiu C. P. B., Methods in Molecular Biology, Springer US, New York, NY, 2021, vol. 2199, pp. 175–189, DOI: 10.1007/978-1-0716-0892-0_11.

31 A. Micsonai, F. Wien, L. Kernya, Y. H. Lee, Y. Goto, M. Réfrégiers and J. Kardos, Accurate secondary structure prediction and fold recognition for circular

dichroism spectroscopy, *Proc. Natl. Acad. Sci.*, 2015, **112**(24), E3095–E3103, DOI: 10.1073/pnas.1500851112.

32 S. Krekic, T. Zakar, Z. Gombos, S. Valkai, M. Mero, L. Zimányi, Z. Heiner and A. Dér, Nonlinear Optical Investigation of Microbial Chromoproteins, *Front. Plant Sci.*, 2020, **11**, 547818, DOI: 10.3389/fpls.2020.547818.

33 T. E. Meyer, E. Yakali, M. A. Cusanovich and G. Tollin, Properties of a water-soluble, yellow protein isolated from a halophilic phototrophic bacterium that has photochemical activity analogous to sensory rhodopsin, *Biochemistry*, 1987, **26**(2), 418–423.

34 Z. Heiner, A. Der, V. Petrov and M. Mero, Nonlinear vibrational spectrometer for bioapplications featuring narrowband 1-μm pulses and a recycled OPA pump beam, *Opt. Express*, 2024, **32**(25), 45029–45040.

35 Z. Heiner, L. Wang, V. Petrov and M. Mero, Broadband vibrational sum-frequency generation spectrometer at 100 kHz in the 950-1750 cm^{-1} spectral range utilizing a $LiGaS_2$ optical parametric amplifier, *Opt. Express*, 2019, **27**(11), 15289–15297.

36 A. G. F. de Beer, J. S. Samson, W. Hua, Z. Huang, X. Chen, H. C. Allen, *et al.*, Direct comparison of phase-sensitive vibrational sum frequency generation with maximum entropy method: Case study of water, *J. Chem. Phys.*, 2011, **135**(22), 224701.

37 M. Sovago, E. Vartiainen and M. Bonn, Determining Absolute Molecular Orientation at Interfaces: A Phase Retrieval Approach for Sum Frequency Generation Spectroscopy, *J. Phys. Chem. C*, 2009, **113**(15), 6100–6106.

38 U. Schade, A. Röseler, E. H. Korte, F. Bartl, K. P. Hofmann, T. Noll, *et al.*, New infrared spectroscopic beamline at BESSY II, *Rev. Sci. Instrum.*, 2002, **73**(3), 1568–1570.

39 A. Veber, L. Puskar, J. Kneipp and U. Schade, Infrared spectroscopy across scales in length and time at BESSY II, *J. Synchrotron Radiat.*, 2024, **31**(3), 613–621.

40 D. Nečas and P. Klapetek, Gwyddion: an open-source software for SPM data analysis, *Open Phys.*, 2012, **10**(1), 181–188.

41 S. Strazdaite, S. J. Roeters, A. Sakalauskas, T. Sneideris, J. Kirschner, K. B. Pedersen, *et al.*, Interaction of Amyloid-β-(1–42) Peptide and Its Aggregates with Lipid/Water Interfaces Probed by Vibrational Sum-Frequency Generation Spectroscopy, *J. Phys. Chem. B*, 2021, **125**(40), 11208–11218.

42 A. V. Mikhonin, N. S. Myshakina, S. V. Bykov and S. A. Asher, UV Resonance Raman Determination of Polyproline II, Extended 2.51-Helix, and β-Sheet Ψ Angle Energy Landscape in Poly-L-Lysine and Poly-L-Glutamic Acid, *J. Am. Chem. Soc.*, 2005, **127**(21), 7712–7720.

43 P. Batys, M. Morga, P. Bonarek and M. Sammalkorpi, pH-Induced Changes in Polypeptide Conformation: Force-Field Comparison with Experimental Validation, *J. Phys. Chem. B*, 2020, **124**(14), 2961–2972.

44 K. Cieślik-Boczula, Alpha-helix to beta-sheet transition in long-chain poly-L-lysine: Formation of alpha-helical fibrils by poly-L-lysine, *Biochimie*, 2017, **137**, 106–114.

45 L. Fu, Z. Wang, B. T. Psciuk, D. Xiao, V. S. Batista and E. C. Y. Yan, Characterization of Parallel β-Sheets at Interfaces by Chiral Sum Frequency Generation Spectroscopy, *J. Phys. Chem. Lett.*, 2015, **6**(8), 1310–1315.

46 J. S. Yoneda, A. J. Miles, A. P. U. Araujo and B. A. Wallace, Differential dehydration effects on globular proteins and intrinsically disordered proteins during film formation, *Protein Sci.*, 2017, **26**(4), 718–726.
47 F. Madzharova, Z. Heiner and J. Kneipp, Surface Enhanced Hyper-Raman Scattering of the Amino Acids Tryptophan, Histidine, Phenylalanine, and Tyrosine, *J. Phys. Chem. C*, 2017, **121**(2), 1235–1242.
48 I. Pascual Robledo, C. Maciel-Escudero, M. Schnell, L. Mester, J. Aizpurua and R. Hillenbrand, Theoretical Description of Infrared Near-Field Spectroscopy of In- and Out-of-Plane Molecular Vibrations in Thin Layers, *ACS Photonics*, 2025, **12**(7), 3782–3793.
49 K. Y. Chiang, F. Matsumura, C. C. Yu, D. Qi, Y. Nagata, M. Bonn, *et al.*, True Origin of Amide I Shifts Observed in Protein Spectra Obtained with Sum Frequency Generation Spectroscopy, *J. Phys. Chem. Lett.*, 2023, **14**(21), 4949–4954.
50 E. C. Y. Yan, L. Fu, Z. Wang and W. Liu, Biological Macromolecules at Interfaces Probed by Chiral Vibrational Sum Frequency Generation Spectroscopy, *Chem. Rev.*, 2014, **114**(17), 8471–8498.
51 M. Okuno and T. Ishibashi, Heterodyne-Detected Achiraland Chiral Vibrational Sum Frequency Generation of Proteins at Air/Water Interface, *J. Phys. Chem. C*, 2015, **119**(18), 9947–9954.
52 E. A. Perets, D. Konstantinovsky, L. Fu, J. Chen, H. F. Wang, S. Hammes-Schiffer, *et al.*, Mirror-image antiparallel β-sheets organize water molecules into superstructures of opposite chirality, *Proc. Natl. Acad. Sci.*, 2020, **117**(52), 32902–32909.
53 M. L. McDermott, H. Vanselous, S. A. Corcelli and P. B. Petersen, DNA's Chiral Spine of Hydration, *ACS Cent. Sci.*, 2017, **3**(7), 708–714.
54 D. Konstantinovsky, E. A. Perets, T. Santiago, L. Velarde, S. Hammes-Schiffer and E. C. Y. Yan, Detecting the First Hydration Shell Structure around Biomolecules at Interfaces, *ACS Cent. Sci.*, 2022, **8**(10), 1404–1414.
55 G. Ladam, C. Gergely, B. Senger, G. Decher, J. C. Voegel, P. Schaaf, *et al.*, Protein Interactions with Polyelectrolyte Multilayers: Interactions between Human Serum Albumin and Polystyrene Sulfonate/Polyallylamine Multilayers, *Biomacromolecules*, 2000, **1**(4), 674–687.
56 L. Richert, Y. Arntz, P. Schaaf, J. C. Voegel and C. Picart, pH dependent growth of poly(L-lysine)/poly(L-glutamic) acid multilayer films and their cell adhesion properties, *Surf. Sci.*, 2004, **570**(1), 13–29.
57 N. Ji, V. Ostroverkhov, C. Y. Chen and Y. R. Shen, Phase-Sensitive Sum-Frequency Vibrational Spectroscopy and Its Application to Studies of Interfacial Alkyl Chains, *J. Am. Chem. Soc.*, 2007, **129**(33), 10056–10057.
58 M. J. Hofmann and P. Koelsch, Retrieval of complex $\chi(2)$ parts for quantitative analysis of sum-frequency generation intensity spectra, *J. Chem. Phys.*, 2015, **143**(13), 134112.